カオスと重力波

早稲田大学
理工学部

前田恵一

序　相対論的力学系

連星系

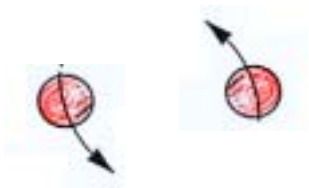

重力波

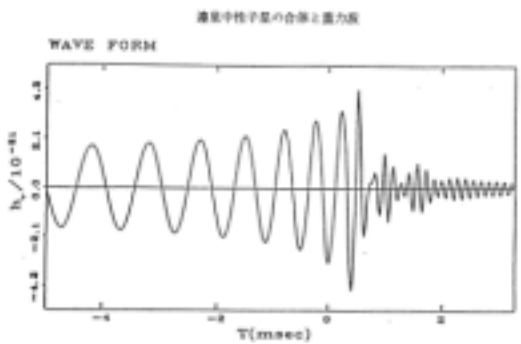

多体系

black holes

Supermassive BH

重力波天文学

template

matched filtering

力学系

ニュートン重力

三体問題（*Poincare*）・・・カオス

⟷ 初期値鋭敏性

一般相対論

非線形偏微分方程式

➡ 新しいタイプのカオス現象

計量（重力ポテンシャル）も非線形

時空のカオス(Bianchi IX)

➡ 相対論的効果

不安定平衡点

テスト粒子のカオス

多体ブラックホール解のまわりの粒子軌道 G. Contopoulos, Proc. R. Soc. London A431, 183 (1990)

一様磁場中のブラックホール解のまわりの粒子軌道 V. Karas & D. Vokrouhlicky, GRG 24, 729 (1992)

多体特異点解のまわりの粒子軌道 Sota,Suzuki,Maeda, CQG 13, 1241 (1996)

Schwarzschild BH の摂動解中の粒子軌道 L. Bombelli and E. Calzetta, CQG 9, 2573 (1992)

Schwarzschild BH のまわりのスピン粒子 Sota,Suzuki,Maeda, PRD 55, 4848 (1997)

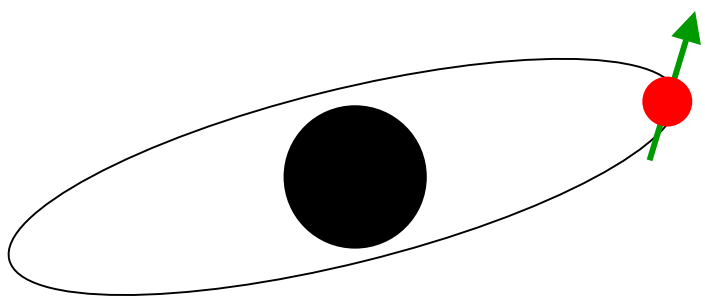

Spinning Test Particle in Schwarzschild BH

S. Suzuki &KM, PRD 55, 4848 (1997)

EOM of a spinning test particle in a relativistic spacetime

Papapetrou, Dixon

$$\frac{dx^\mu}{d\tau} = v^\mu,$$

$$\frac{Dp^\mu}{D\tau} = -\frac{1}{2} R^\mu{}_{\nu\rho\sigma} v^\nu S^{\rho\sigma},$$

$$\frac{DS^{\mu\nu}}{D\tau} = p^\mu v^\nu - p^\nu v^\mu,$$

$$p_\mu S^{\mu\nu} = 0. \qquad v^\mu = N\left[u^\mu + \frac{1}{2\mu^2\Delta} S^{\mu\nu} u^\lambda R_{\nu\lambda\rho\sigma} S^{\rho\sigma}\right],$$

$$\Delta = 1 + \frac{1}{4\mu^2} R_{\alpha\beta\gamma\delta} S^{\alpha\beta} S^{\gamma\delta},$$

$$N = \left[1 - \frac{1}{4\Delta^2\mu^2} S_{\mu\nu} u_\lambda S_{\rho\sigma} R^{\nu\lambda\rho\sigma} S^{\mu\alpha} u^\beta S^{\gamma\delta} R_{\alpha\beta\gamma\delta}\right]^{-1/2}$$

保存量

$\mu^2 = -p_\nu p^\nu$ **質量**　　$S^2 \equiv \frac{1}{2} S_{\mu\nu} S^{\mu\nu}$ **スピン（自転）**

$$C \equiv \xi^\mu p_\mu - \frac{1}{2} \xi_{\mu;\nu} S^{\mu\nu}$$

$\xi_{(t)}$

$$E = -C_{(t)} = -p_t - \frac{M}{r^2} S^{tr}, \quad \textbf{エネルギー}$$

$\xi_{(\phi)}$

$$J_z = C_{(\phi)} = p_\phi - r(S^{\phi r} - r S^{\theta\phi} \cot\theta) \sin^2\theta.$$

全角運動量の z 成分

Schwarzschild 時空

$$ds^2 = -f(r)dt^2 + f(r)^{-1}dr^2 + r^2(d\theta^2 + \sin^2\theta d\phi^2)$$

$$f = 1 - \frac{2M}{r}$$

$$(J_x, J_y, J_z) = (0, 0, J > 0),$$

“有効ポテンシャル” 運動可能領域

$$V_{(\pm)}(r, \theta; J_z, \mathcal{S}) = \mu f^{\frac{1}{2}}(1 + \Lambda_{(\mp)}^2)^{\frac{1}{2}} + \frac{M}{r}\Lambda_{(\mp)}\left(\mathcal{S}^2 - \frac{J^2\cos^2\theta}{1 + \Lambda_{(\mp)}}\right)^{\frac{1}{2}},$$

$$\Lambda_{(\pm)} = -\frac{mJr\sin\theta}{\mu^2 r^2 - \mathcal{S}^2} \pm \left[\frac{\mu^2 J^2 r^2 \sin^2\theta}{(\mu^2 r^2 - \mathcal{S}^2)^2} - \frac{\left(J^2 - \frac{2MJ^2}{r}\cos\theta - \mathcal{S}^2 f\right)}{\mu^2 r^2 - \mathcal{S}^2}\right]^{\frac{1}{2}}.$$

有効ポテンシャル（赤道面）

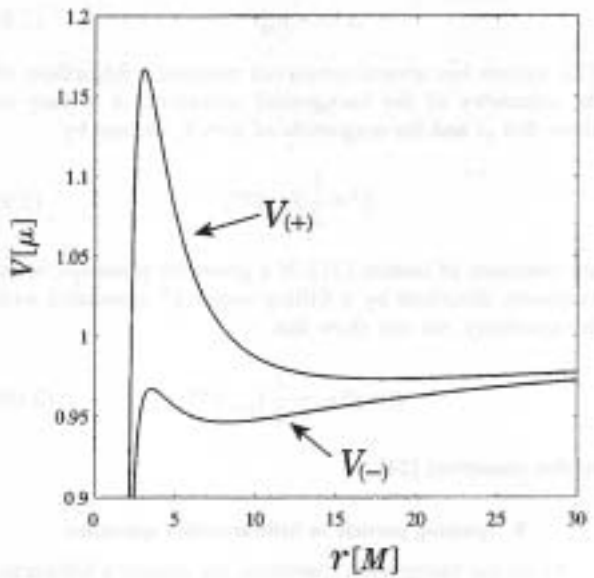

FIG. 1. The "effective potential" $V_{(\pm)}$ on the equatorial plane for $J=4\mu M$ and $S=1\mu M$. We see that the particle in $V_{(-)}$ moves in the region closer to the event horizon ($r=2M$) than that in $V_{(+)}$.

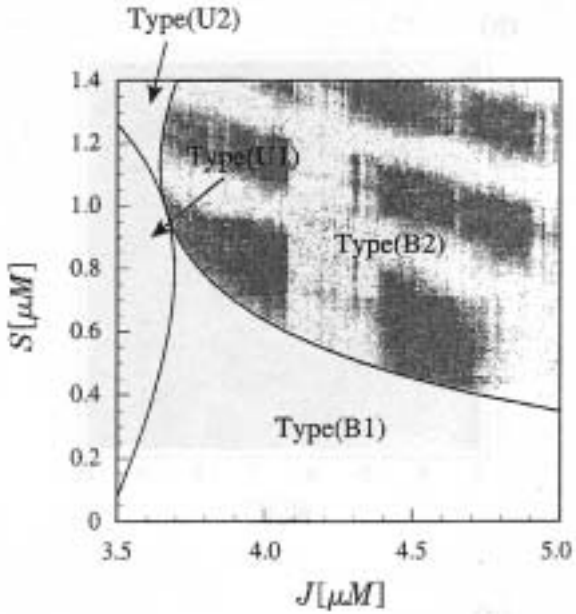

FIG. 3. The types of the "effective potential" are classified by J and S. The value of S at the bottom end of the type (U2) region is slightly smaller than $1\mu M$.

全角運動量とスピンが平行 (−) ・反平行 (+)

***J-M* パラメータ面**

有効ポテンシャル　（等高線）

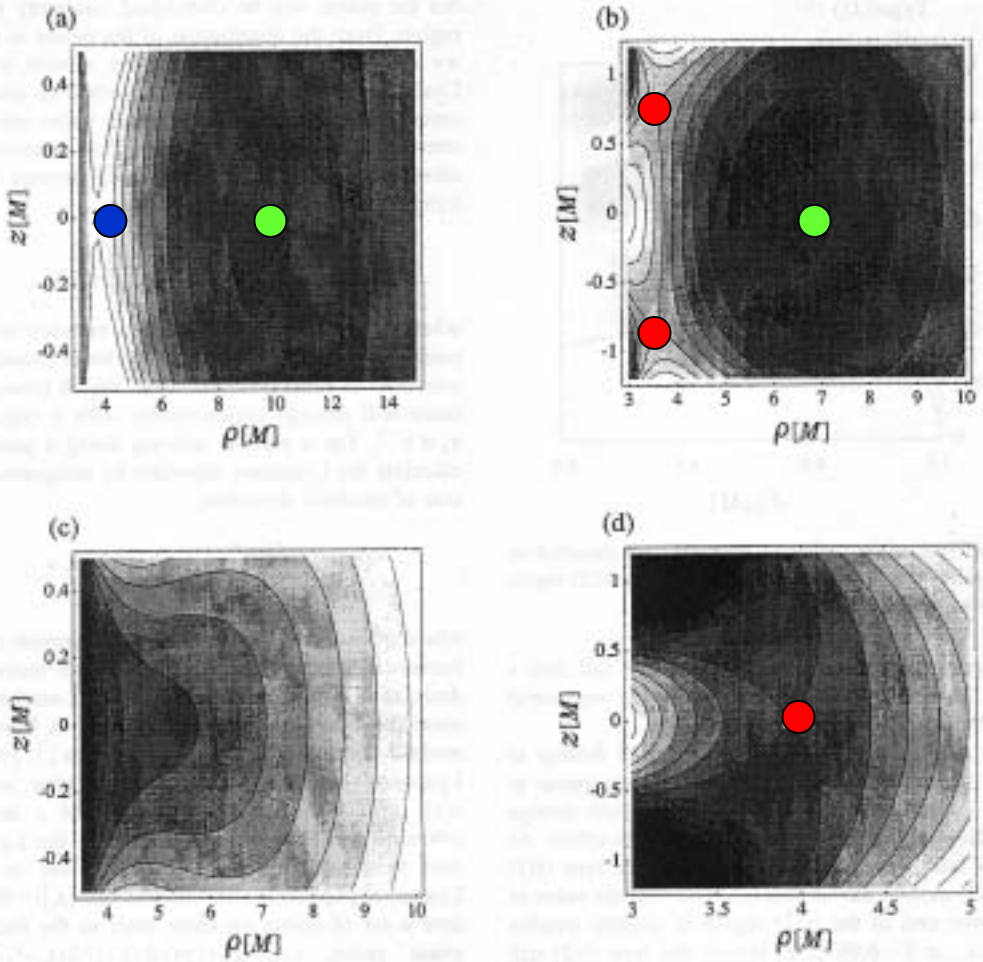

FIG. 2. Four different types of the "effective potential" V. The saddle point of the potential is marked by a cross. (a) Only one saddle point exists on the equatorial plane. This potential is similar to that for a spinless particle. Chaos never occurs in this case. (b) Two saddle points are found on both sides of the equatorial plane. The orbit can be chaotic. (c) When J is very small, the centrifugal force is too small to balance with the gravity and then no bound region is found. This potential is also similar to that for a spinless particle. (d) This also has no bound region. But its shape is different from that of (c). There exists a saddle point on the equatorial plane. This point is locally minimal in the r direction but maximal in θ direction. The particle will eventually fall into the black hole after leaving the equatorial plane.

● 安定

● 不安定

● サドル

ポアンカレ写像

$J = 4\mu M$

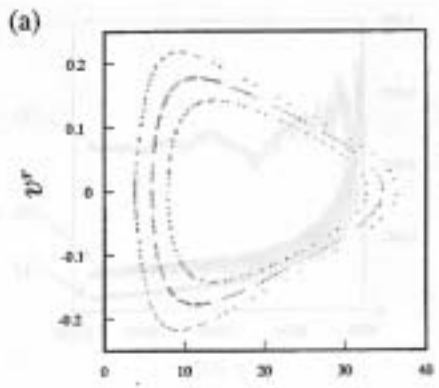

$S = 0.4\mu M$

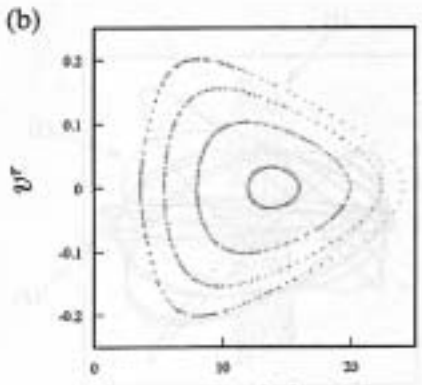

$S = 0.6\mu M$

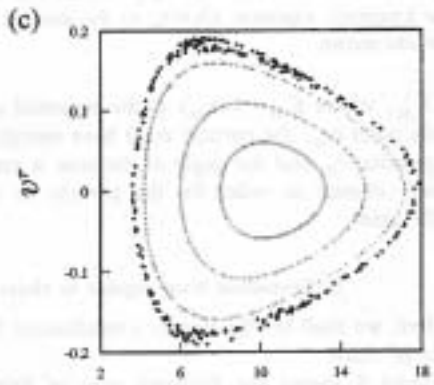

$S = 0.8\mu M$

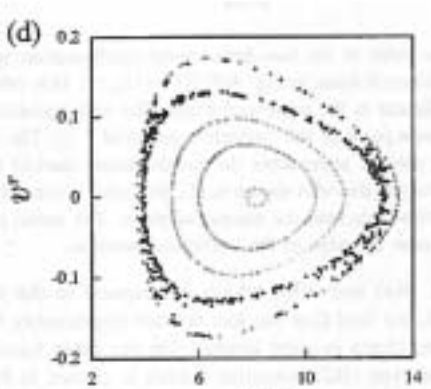

$S = 1\mu M$

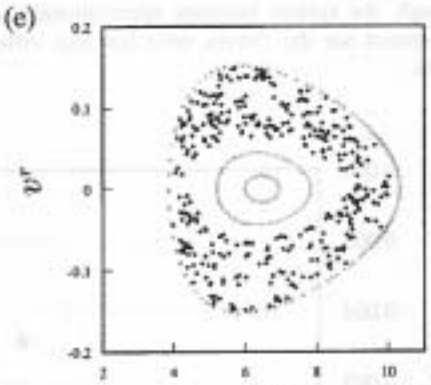

$S = 1.2\mu M$

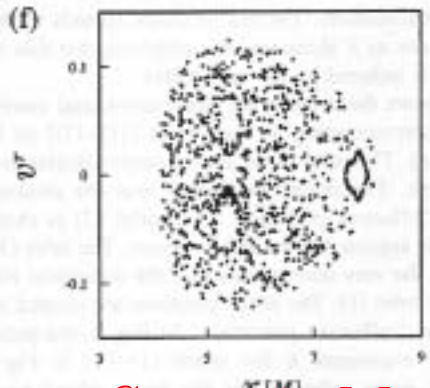

$S = 1.4\mu M$

FIG. 4. The Poincaré maps for various values of S. All orbits have the total angular momentum $J = 4.0\mu M$. We set $p^r = 0$ initially. (a) $S = 0.4\mu M$ and $E = 0.976\,983\,96\mu$: The initial position for each torus is $r_0 = 3.8$, 6.0, and $8.0M$. (b) $S = 0.6\mu M$, $E = 0.967\,309\,99\mu$, and the initial position is $r_0 = 3.6$, 5.5, 8.0, and $12.0M$. (c) $S = 0.8\mu M$, $E = 0.958\,155\,68\mu$, and $r_0 = 3.7$, 4.2, 6.0, and $8.0M$. (d) $S = 1.0\mu M$, $E = 0.947\,381\,62\mu$, and (1) $r_0 = 5M$, (2) $3.9M$(chaotic), (3) $3.72M$. The orbits in two-dimensional configuration space are shown in Fig. 5. (e) $S = 1.2\mu M$, $E = 0.935\,455\,65\mu$, and $r_0 = 3.86$, 4.2, 5.2, and $6.0M$. (f) $S = 1.4\mu M$, $E = 0.922\,929\,41\mu$, and $r_0 = 4.5$, 5.0, 5.7, and $7.6M$. Very strong chaos occurs in this case, although it may be unrealistic.

Lyapunov exponent　　λ：２つの軌道が相空間で指数的に離れていく割合

$$dX \sim \exp[\lambda t]$$

３軌道

(1)　赤道面にほぼ垂直
(2)　サドル近くを通る軌道
(3)　ほぼ赤道面上

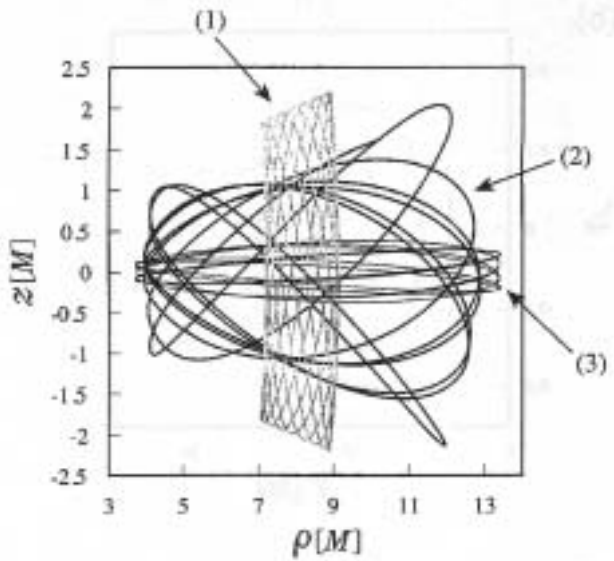

FIG. 5. The orbit in the two-dimensional configuration space corresponding to each torus in Fig. 4(d) [(1)–(3)]. (1) This orbit is almost perpendicular to the equatorial plane. The initial position is near the minimum point of the "effective potential." (2) The chaotic orbit. The particle approaches the saddle points marked by a cross. (3) Contrary to the orbit shown in (1), this orbit is constrained in the very narrow area near the equatorial plane. The initial position is located near the edge of the "effective potential."

カオス的

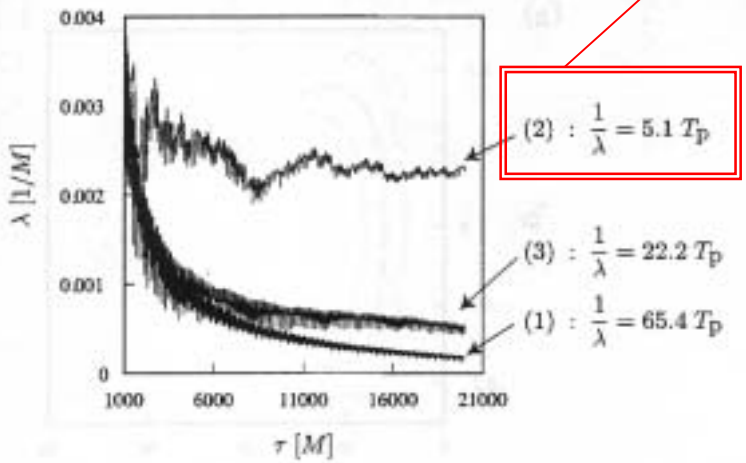

FIG. 6. The Lyapunov exponent of each orbit shown in Fig. 5. We find that the orbit (2) is strongly chaotic. The ratio of the inverse Lyapunov exponent $1/\lambda = \tau_\lambda$ to the average orbital period T_p is also shown.

Lyapunov exponent

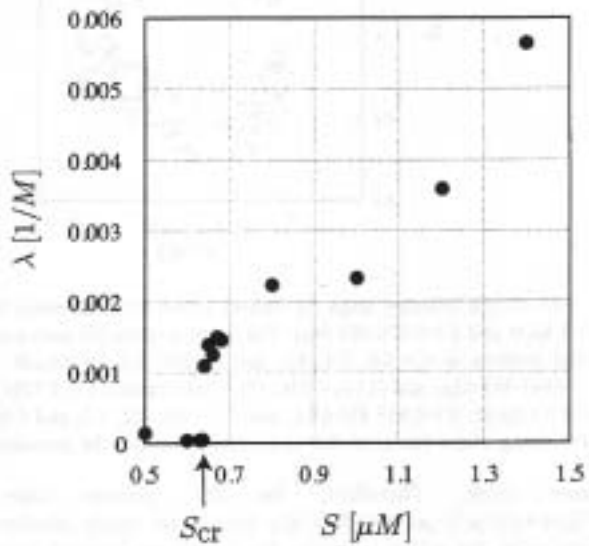

FIG. 7. The Lyapunov exponent λ in terms of the value of spin S. When S becomes larger than the critical value $S_{cr} \sim 0.635 \mu M$, beyond which we find chaos, λ increases rapidly. This supports the notion of a critical value of the spin for occurrence of chaos.

$$S > S_{min} = 0.635 \mu M$$

$$\Rightarrow \quad \lambda > 0$$

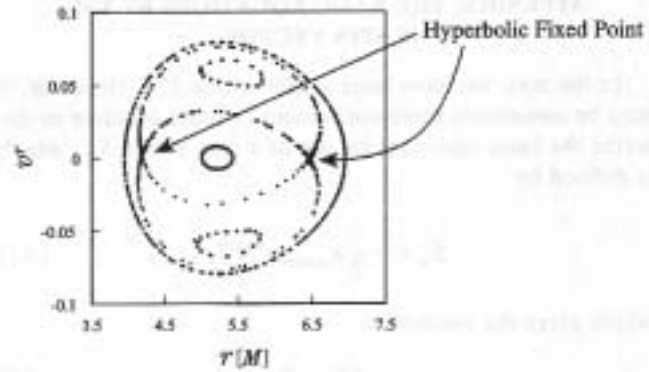

FIG. 8. The classification of the orbits for $J = 3.81 \mu M$, $S = 1 \mu M$, and $E = 0.923 \mu$. We find two separatrix [type (iv)] which divide three types of stable orbits [types (i)–(iii)]. There exists a heteroclinic orbit starting from one hyperbolic fixed point to the other fixed point, which may cause the present chaotic behaviors.

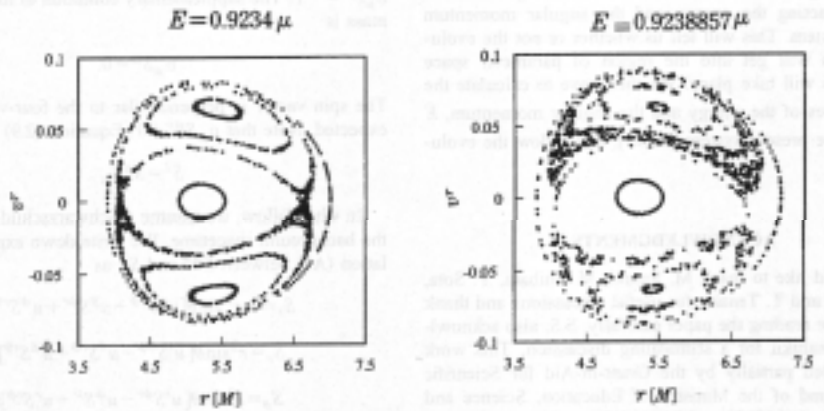

FIG. 9. When the energy increases from that in Fig. 8, the torus gradually spreads out around the heteroclinic orbit in the Poincaré map.

カオス力学系からの重力波

スピンテスト粒子の場合

S. Suzuki&K. Maeda, PRD 61, 024005 (1999)

連星系合体（**2 PN＋2.5PN radiation reaction**）

J. Levin, PRL, 84, 3515 (2000)

J.D. Schnittman & F.A. Rasio, PRL, 87, 121101 (2001)

N.J. Cornish & J. Levin, PRL, 89, 179001 (2002)

連星系合体におけるカオス:あまり重要でない？

重力波

３つの軌道

$S = 1\mu M$

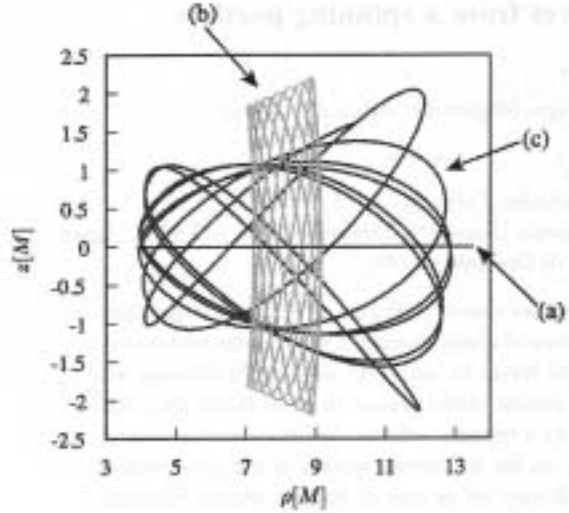

(a) “楕円”軌道
(b) 赤道面にほぼ垂直
(c) 鞍点近くを通過する軌道
（カオス的）

四重極公式

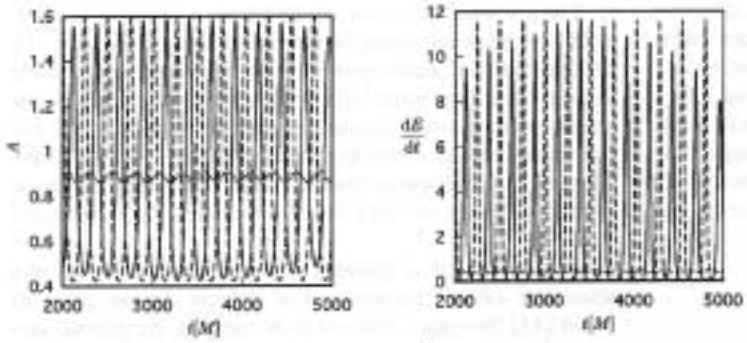

重力波の振幅

FIG. 2. (i) The average amplitude of the gravitational waves for all direction for orbit (a) (dashed line), orbit (b) (dotted line), and orbit (c) (solid line). (ii) The energy emission rate of the gravitational waves. These are normalized by the value for the circular orbit in the same "effective potential," which is constant. The amplitude and emission rate for orbit (a) is slightly larger than those for the chaotic case.

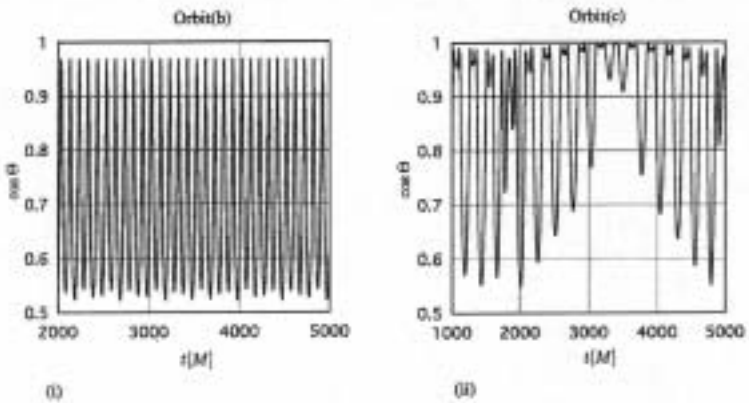

軌道面の歳差運動

FIG. 3. The precession of the orbital plane for (i) orbit (b) (quasiperiodical case) and (ii) orbit (c) (chaotic case).

波形

＋モード　　×モード

赤道面上の観測者

(a)

(b)

(c)

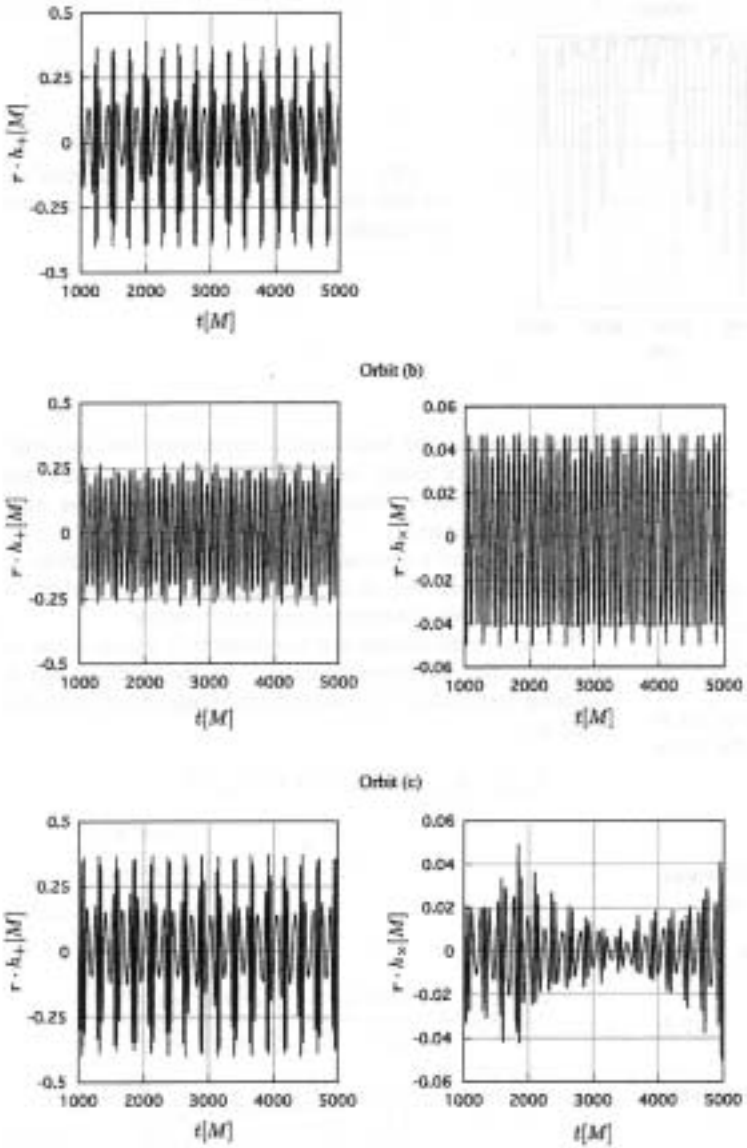

FIG. 4. The gravitational wave forms of the plus mode and the cross mode for the observer on the equatorial plane. The top panel shows the gravitational wave for orbit (a). The cross mode vanishes. The middle panels show the gravitational waves for orbit (b). The bottom ones show these for orbit (c).

エネルギー・スペクトル

円軌道　　“楕円”軌道 (a)

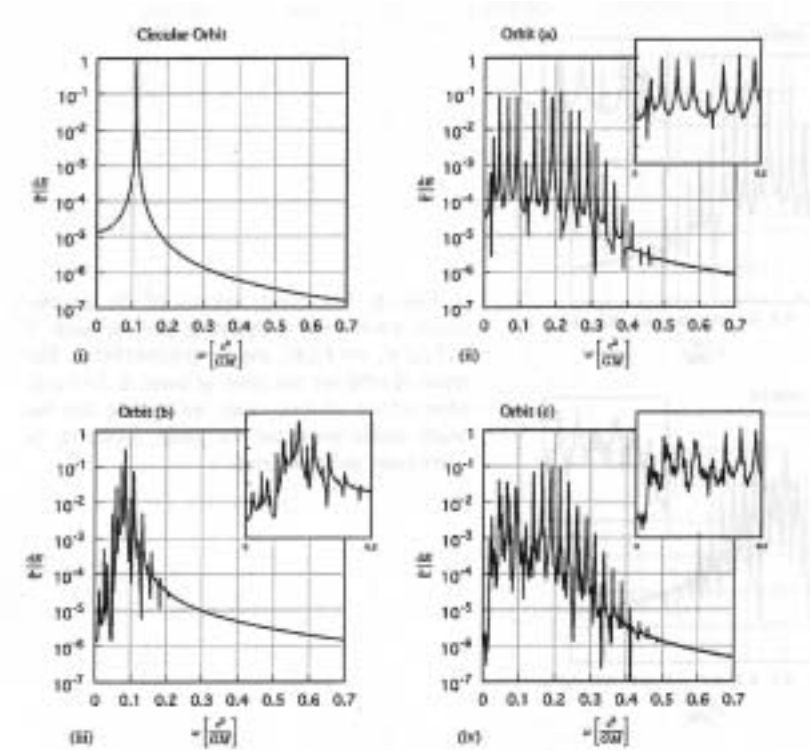

(b) 赤道面に垂直　　カオス的軌道 (c)

円軌道：**sharp peak**

“楕円”軌道:
sharp peaks in a broad band

FIG. 5. The energy spectra of the gravitational wave for each case. (i) The energy spectra for the circular orbit. The frequency of the peak is $\omega = 0.1148[c^3/GM]$. (ii)–(iv) The energy spectrum for each orbit. The values in these cases are normalized by the peak value for the circular orbit. The small boxes attached to each figure show the enlargement of the low frequency region. For orbit (c) (chaotic), the spectra is noisy and each spike is broadened compared with the other cases.

赤道面に垂直:
randam sharp peaks in a narrow band

カオス的軌道:
randam peaks in a broad band

$S = 1.2\ \mu M$

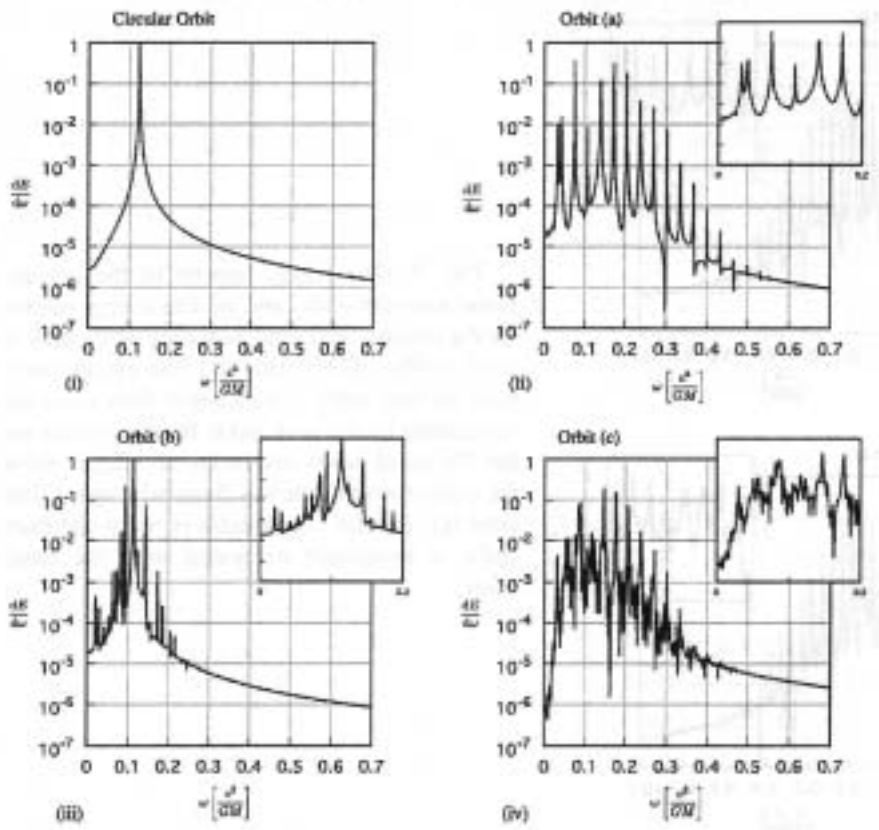

FIG. 6. The energy spectra of the gravitational wave from a spinning particle with $S = 1.2\mu M$, $J = 4\mu M$, and $E = 0.93545565\mu$. The types of orbit are the same as those in $S = 1\mu M$ case. In (iv) (chaotic case), we can see that the small spikes exist and the peaks appearing in other cases are broadened.

Post-Newtonian

2PN

2.5PN

$$\ddot{\mathbf{r}} = \mathbf{a}_{\rm PN} + \mathbf{a}_{\rm SO} + \mathbf{a}_{\rm SS} + \mathbf{a}_{\rm RR}$$

$$\dot{\mathbf{S}}_1 = \mathbf{\Omega}_1 \times \mathbf{S}_1 \qquad \dot{\mathbf{S}}_2 = \mathbf{\Omega}_2 \times \mathbf{S}_2$$

M_2/M_1=1.4/10

S_1=S_2=0

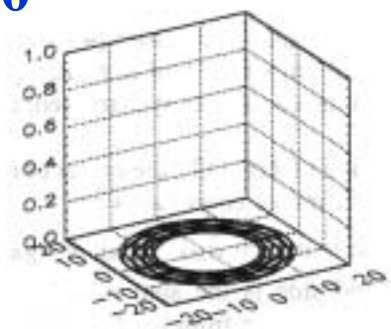

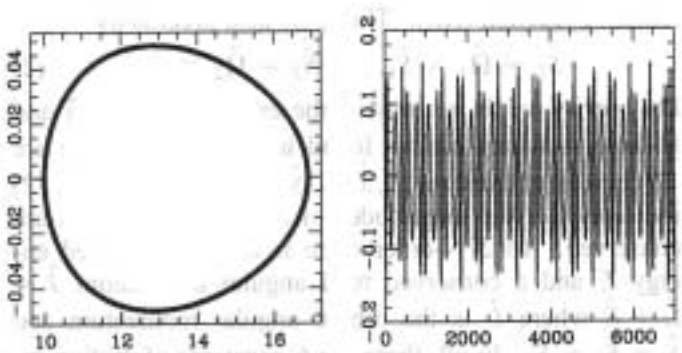

FIG. 1. The pair has mass ratio $m_2/m_1 = 1.4/10$ and no spins. The initial conditions are $x_i/m = 10$, $\dot{y}_i = 0.3$, and $z_i = 0$. Time is measured in units of the total mass m. Top: A 3D view of the orbit. Lower left: The smooth phase space curve in the $(r, \dot{r})$ plane. Lower right: The waveform h_+.

S_1= 1.0 M_1^2

S_2= 0.7 M_2^2

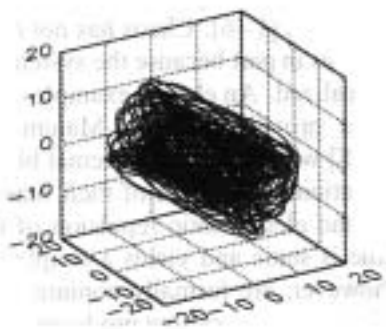

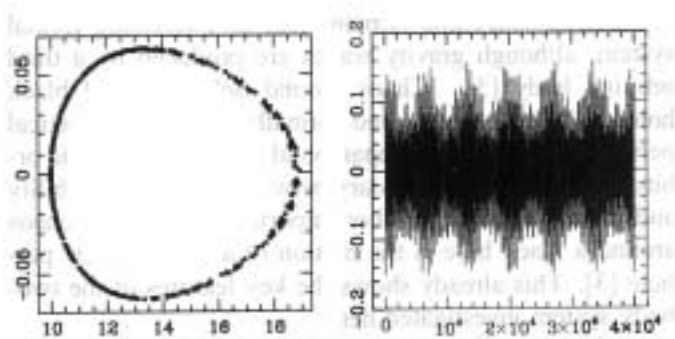

FIG. 2. The pair has mass ratio $m_2/m_1 = 1.4/10$ and spins $S_1 = m_1^2$, $S_2 = 0.7m_2^2$. The initial conditions are $x_i/m = 10$, $\dot{y}_i = 0.3$, and $z_i = 0$. The initial angles are $\theta_1 = \theta_2 = 45°$. Top: A 3D view of the orbit. Lower left: The surface of section in the $(r, \dot{r})$ plane. Lower right: The waveform h_+.

fractal basin

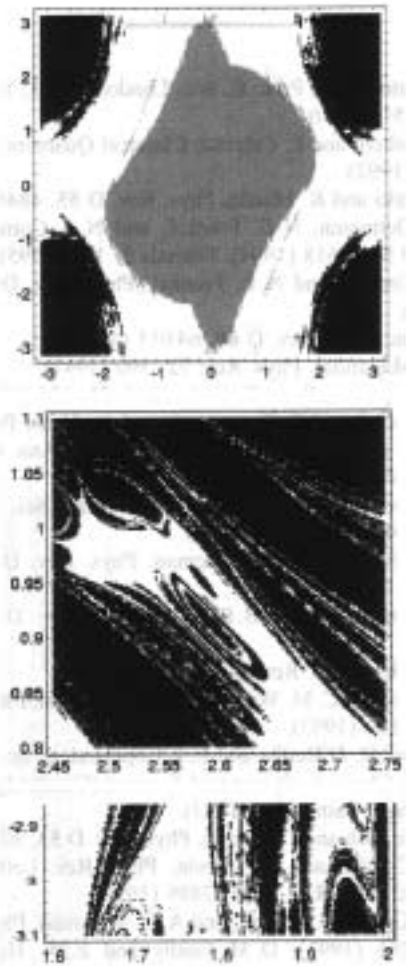

FIG. 3. Top: The fractal basin boundaries for pairs with $m_2/m_1 = 1/3$ and $S_1/m_1^2 = S_2/m_2^2 = 0.6$. All orbits begin with $x_1/m = 5$, $\dot{y}_i = 0.45$. The initial angles (θ_1, θ_2) are varied. The axes are labeled in radians. There are 200×200 orbits shown. The middle and bottom panels are details of the upper panel.

black: coalesce

grey: separate (r>1000M)

white: stable motion

$\theta_1 = 10°; \theta_2 = 128°$ $\theta_1 = 10°; \theta_2 = 131°$

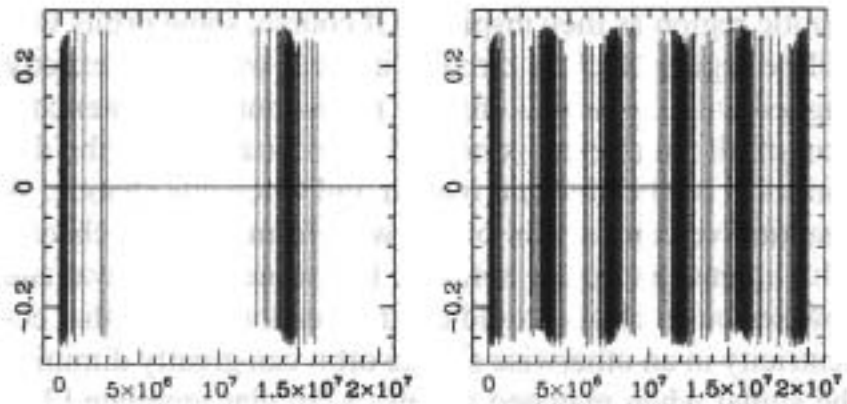

FIG. 4. The waveform h_+ for pairs selected from the initial conditions in Fig. 3. Both orbits begin with $\theta_1 = 10°$. The left panel began with $\theta_2 = 128°$ while the right panel began with $\theta_2 = 131°$. The extreme angles were randomly chosen from the fractal set for illustration. Chaos is seen with more temperate angles as in Fig. 2.

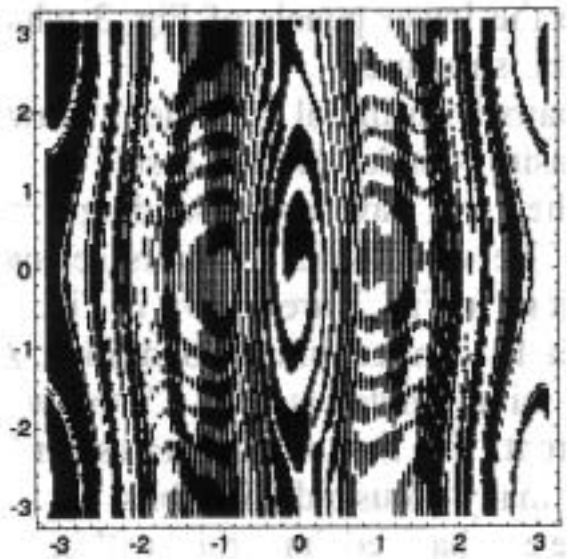

FIG. 5. The fractal basin boundaries with dissipation included. The parameters are $m_2/m_1 = 1.4/10$ and spins $S_1 = m_1^2$ and $S_2 = 0.7m_2^2$. The orbits begin with $x_i/m = 26$, $\dot{y}_i = 0.15$, and $z_i = 0$. The pair can execute anywhere from 0 to $\mathcal{O}(40)$ orbits before coalescence. The initial angles (θ_1, θ_2) are varied from $-\pi$ to π. There are 300×300 orbits shown.

fractal basin with dissipation

reanalysis **2PN+2.5PN radiation reaction**

テスト粒子近似

$M_2/M_1 = 10^{-4}$ $S_1 = 0$ $S_2 = 1.4 \times 10^4 M_2^2$

(a) $L = 1.485\ \mu M$ **(b) $L = 1.53\ \mu M$**

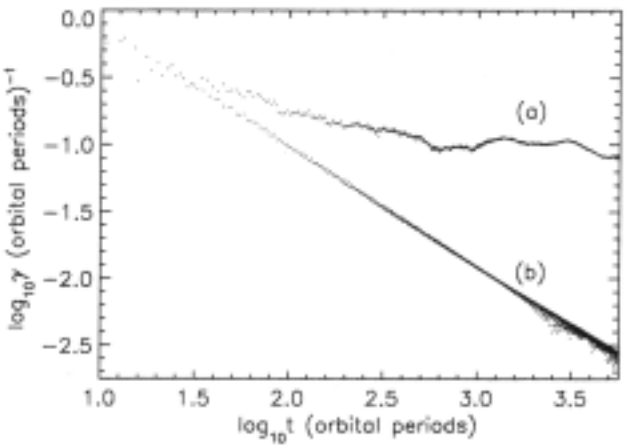

FIG. 1. Lyapunov exponent γ for test-particle orbits around a black hole. The orbits in case (a) are chaotic, with γ approaching a positive value corresponding to a divergence time of $t_L \sim 10$ orbital periods. The regular orbits in case (b) diverge linearly in time so that $\gamma(t) \to 0$.

Lyapnov exponent

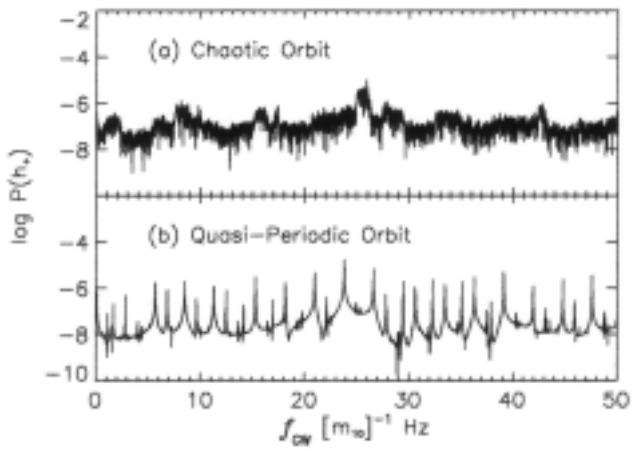

FIG. 2. Power spectra of the GW signal $h_+(t)$ for the same two cases as in Fig. 1. The chaotic system in (a) produces broadband noise while the quasiperiodic orbit (b) exhibits sharp spectral lines. The GW frequency is given in units of m_{10}^{-1} Hz, where $m_{10} = m/10M_\odot$.

spectrum

$10M_\odot$ black hole binary $S_1=M_1^2$ $S_2=M_2^2$

Lyapunov exponent

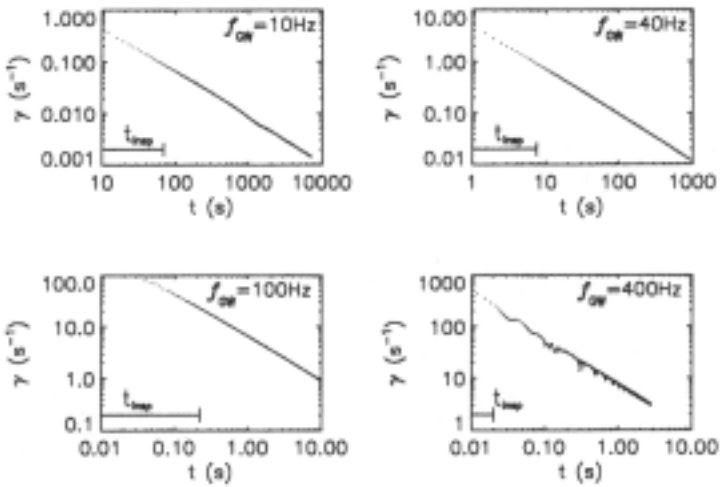

FIG. 3. Lyapunov exponent $\gamma(t)$ for different stages in the inspiral of two maximally spinning $10M_\odot$ black holes: $f_{GW} = 10$ Hz, $r/m = 47.25$, $t_{insp} = 69$ s; $f_{GW} = 40$ Hz, $r/m = 18.75$, $t_{insp} = 7.5$ s; $f_{GW} = 100$ Hz, $r/m = 9.2$, $t_{insp} = 0.2$ s; $f_{GW} = 400$ Hz, $r/m = 4.0$, $t_{insp} = 0.01$ s. No evidence for chaos is seen, with $t_L = 1/\gamma \gg t_{insp}$ in all cases.

スペクトル

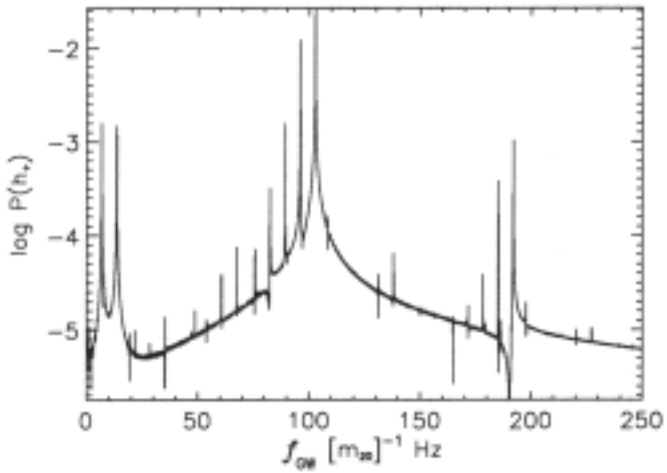

FIG. 4. Power spectrum of the GW signal $h_+(t)$ calculated from the initial conditions of Fig. 3 at the stage in the inspiral where $f_{GW} = 100$ Hz. The frequency is in units of m_{20}^{-1} Hz, where $m_{20} = m/20M_\odot$. The sharp lines in the spectrum confirm that the orbit is regular.

no chaos

Lyapunov Exponent

束縛条件が存在 ⟹ 相空間のデカルト座標距離ではない

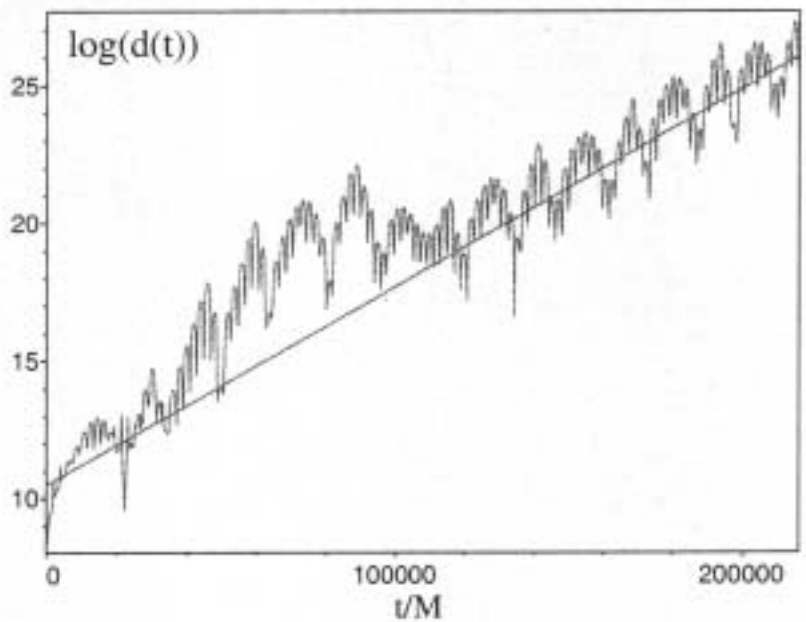

FIG. 1 (color online). Determining the Lyapunov exponent for an orbit taken from Fig. 3 of Ref. [2].

今後の課題：

ブラックホール多体系

多重極の影響 

カオス力学系からの重力波の特徴の解明：現在解析中

phase cancellation ?

カオスが重力波観測に与える影響

カオス力学系特有の振る舞い  より詳細なデータ

質点＋ディスク(Newtonian)

重力波のスペクトル

ディスクの厚さ

厚い ⟶ 薄い

面密度一定

カオス的